A Rotating PET Scanner Using BGO Block Detectors: Design, Performance and Applications

David W. Townsend, Martin Wensveen, Larry G. Byars, Antoine Geissbuhler, Henri J. Tochon-Danguy, Anne Christin, Michel Defrise, Dale L. Bailey, Sylke Grootoonk, Alfred Donath and Ronald Nutt

Division of Nuclear Medicine, University Hospital, Geneva, Switzerland; CTI/Siemens PET Systems, Knoxville, Tennessee; Division of Nuclear Medicine, Vrije Universiteit, Brussels, Belgium; Division of Nuclear Medicine, Royal Prince Alfred Hospital, Sydney, Australia; and MRC Cyclotron Unit, Hammersmith Hospital, London, United Kingdom

Recent advances in fully three-dimensional reconstruction for multi-ring PET scanners have led us to explore the potential of a prototype scanner based on the rotation of two opposing arrays of BGO block detectors. The prototype contains only one-third of the number of detectors in the equivalent full ring scanner, resulting in reduced cost. With a lower energy threshold at 250 keV, the absolute efficiency of the scanner is 0.5% and the scatter fraction is 35% for a 20-cm cylinder. Transaxial and axial spatial resolution is about 6 mm. The maximum noise equivalent count rate estimated for a 15-cm diameter cylinder is 36,000 cps at a concentration of 26 kBq/ml. The minimum scan time for a ^{18}F-fluoro-2-deoxyglucose (FDG) brain study is 55 sec. The camera has been validated for clinical applications using both FDG and ^{82}Rb.

J Nucl Med 1993; 34:1367–1376

During the late seventies and early eighties, the potential of PET camera designs based on the rotation of a pair of opposing two-dimensional, area detectors was explored by a number of groups (1–5). These investigations also stimulated the development of fully three-dimensional reconstruction algorithms (6–8). However, the technology that was available at that time for constructing area detectors had low sensitivity and resulted in PET scanners with only limited clinical interest (9,10). Although the approach may still be interesting for small animal imaging (11,12), it has, with few exceptions (13), essentially been abandoned for human studies in favour of PET scanners based on multiple stationary rings of small bismuth germanate (BGO) crystals.

Presently, most state-of-the-art commercial PET scanners comprise multiple rings of BGO detectors, each ring consisting of 400–500 individual crystals. Until recently,

the rings were shielded by interplane septa so that active coincidence channels were limited to those between detectors either in the same ring or in adjacent rings. However, multi-ring scanners have now become available with retractable septa (14) and coincidences can be acquired between detectors in any two rings. Data acquired with the septa retracted are reconstructed using a fully three-dimensional reconstruction algorithm (15,16) similar in approach to that originally developed for rotating area detectors (6). With septa retracted (three-dimensional mode), the overall sensitivity of a 16-ring scanner is increased by a factor of six compared to operation with septa.

The possibility of increasing sensitivity by operating in three-dimensional mode introduces an additional degree of flexibility in selecting the appropriate detector configuration. For example, consider a single ring of 384 detectors. To adequately cover a transaxial brain section, suppose that each detector is in coincidence with a fan of 76 detectors opposite. The total number of active coincidence channels, or lines of response (LORs), in such a configuration is 14592 (i.e., 76 × 192). Alternatively, if 380 detectors are arranged instead as two opposing arrays of 38 (transaxial) × 5 (axial), the number of active LORs in three-dimensional mode would be 36100 (i.e., (38 × 5)^2). Although in the latter case, the detector arrays would have to be rotated to collect data for a full three-dimensional reconstruction, the number of active LORs is actually greater than when the same detectors are arranged in a single ring. Both configurations cover the same transaxial field of view, and the rotating arrays have a larger axial field of view.

Although they have potentially greater intrinsic sensitivity, rotating arrays have a number of obvious drawbacks. These include the requirement for mechanical motion, the possibility of tracer redistribution during the scan and the increased sensitivity of unshielded, two-dimensional detector arrays to scattered photons. In order to explore the advantages and disadvantages of such a detector configuration, we have developed a prototype PET scanner based on rotating 16 partial rings of BGO detectors (17). In addi-

tion to the recent advances in three-dimensional reconstruction algorithms (14–16), renewed interest in rotating arrays arises because, when compared with the technology used in earlier efforts (1–5), BGO detectors offer state-of-the-art sensitivity, spatial resolution and count rate performance. In the design we have explored, the detectors are mounted as two opposing arcs, each arc subtending an angle of 60°. The total number of detectors (2048) is one-third the number of detectors in the equivalent, full-ring scanner. The rotating configuration therefore represents a significant reduction in cost.

The number of rotational positions at which data are acquired, and the step between these positions, is dependent upon the imaging field of view (FOV) required for the study. The smaller the angular step between acquisition positions, the larger the FOV imaged. A LOR is defined by a position (e.g., distance from the center of the scanner, s) and direction (ϕ), and with this scanner, coincidences for the same LOR may be acquired with the detector arrays at a number of different angular positions, i.e., the same (s, ϕ) may occur with more than one detector pair. As will be seen, this results in variable sensitivity in the transaxial FOV.

Coincidences are stored in the acquisition memory in sinograms. A sinogram is a two-dimensional matrix in which each LOR has an address specified by the two coordinates (s, ϕ) (18). During the scan, sinograms are progressively assembled from data collected at each rotational position, and coincidences acquired between detectors within the same ring or in any two different rings are stored in 256 (16 × 16) separate sinograms. A sinogram containing coincidences between detectors in the same ring is a *direct plane* sinogram, whereas a sinogram containing coincidences between detectors in different rings is a *cross plane* sinogram (18). These sinograms correspond to a set of two-dimensional projections of the tracer distribution, which must be reconstructed using a fully three-dimensional reconstruction algorithm (15). For a full-ring scanner, we have implemented such an algorithm based on the three-dimensional filtered backprojection approach (16). The same software is used to reconstruct the data from the rotating scanner.

Any scanner requires that the radioisotope in the FOV does not redistribute during the scan. For a full-ring scanner, isotope redistribution will result in some spatial blurring in the image, whereas for a rotating scanner it will result in the acquisition of inconsistent projection data leading to artifacts in the reconstructed image. A rotating scanner cannot therefore be used to image rapidly changing isotope distributions. For a 20-cm diameter FOV, the minimum scan duration with this prototype is 55 sec. Slowly varying tracer distributions are required in order to obtain accurate time-activity curves. This has been possible for ^{18}F-fluoro-deoxyglucose (FDG) uptake in the brain.

We present the design characteristics and performance parameters of the prototype scanner. Operation of the scanner will be illustrated by some clinical applications using FDG to image glucose uptake in the brain, heart and tumors, and ^{82}Rb to image the heart.

MATERIALS AND METHODS

Block Detectors

Physically, the detectors are constructed by cutting a BGO block (19) into an array of 8 × 8 individual detectors, each of dimension 5.6 × 6.45 × 30 mm. The block is viewed by four photomultiplier tubes and Anger-type logic is used to localize the interaction. The measured energy resolution of the blocks is 23% at 511 keV (20). Four of these blocks are mounted on a single-base plate, together with the electronics for position-encoding, timing and energy discrimination. This basic modular unit, called a bucket, covers an arc length of about 20 cm transaxially and 5.4 cm axially. Since the block is cut into eight detectors both axially and transaxially, a complete ring of buckets is eight rings of individual detectors.

A standard commercial tomograph, such as the ECAT 953B (20), consists of two adjacent rings of 12 buckets, with a diameter of 76 cm between opposing crystals. This represents 16 rings (2 × 8 per block) each of 384 detectors (12 buckets × 4 blocks/bucket × 8 detectors/block). The axial length of the scanner is the width of two blocks, i.e., 10.8 cm. The rotating scanner described in this paper has eight buckets of these state-of-the-art detectors, arranged in two groups of four (Fig. 1), so as to have the same axial coverage as the 953B. Each detector ring therefore contains 128 detectors, one-third of the number in the 953B. The effective ring diameter is 76 cm and the patient entry port is 55 cm. Sinogram input to the reconstruction software is essentially identical to that acquired by the full-ring 953B.

Imaging FOV

A pair of buckets operating in coincidence acquires data from LORs lying within a diamond-shaped region of a sinogram. This is illustrated in Figure 2A, where for simplicity the "bucket" contains only eight detectors. For N detectors in a bucket, the axes of the diamond are N radial samples (s) by 2N-1 angular samples (ϕ). In practice, interpolation is used to rebin the samples to obtain 2N-1 radial samples at N angular samples (18). For a correct reconstruction, all radial samples are required at each angular sample. For a single diamond region, this condition is only satisfied for the radial sample at the center of the sinogram. In general, the number of radial samples (FOV width) for which this condition is satisfied depends upon the number of buckets in coincidence with a single bucket. For the 953B, each bucket is in coincidence with an opposing arc of seven buckets.

For this camera, the detectors in coincidence acquire data from LORs located within four sinogram diamonds at a fixed position of the buckets, as shown in Figure 2B, which also form a diamond-shaped region. The dimensions of this region are 127 radial samples by 64 angular samples. The radial sampling distance is 3.1 mm. As the detectors rotate, the diamond-shaped region is displaced down the ordinate (ϕ) axis of the sinogram. However, the actual size of the useful FOV depends upon the extent of the overlap of this region from one acquisition position to the next. The two extreme situations are a step of two buckets, resulting in nonoverlapping regions and a FOV of one radial sample, to a step of one detector (i.e., one angular sample), which results in a FOV of 127 radial samples (about 39 cm). Intermediate steps can be chosen according to the size of the FOV required. However, it is evident that some LORs are acquired at more than one angular position. For a step of one detector, the LORs at the center of the projection are acquired 64 times more often than the LORs at the
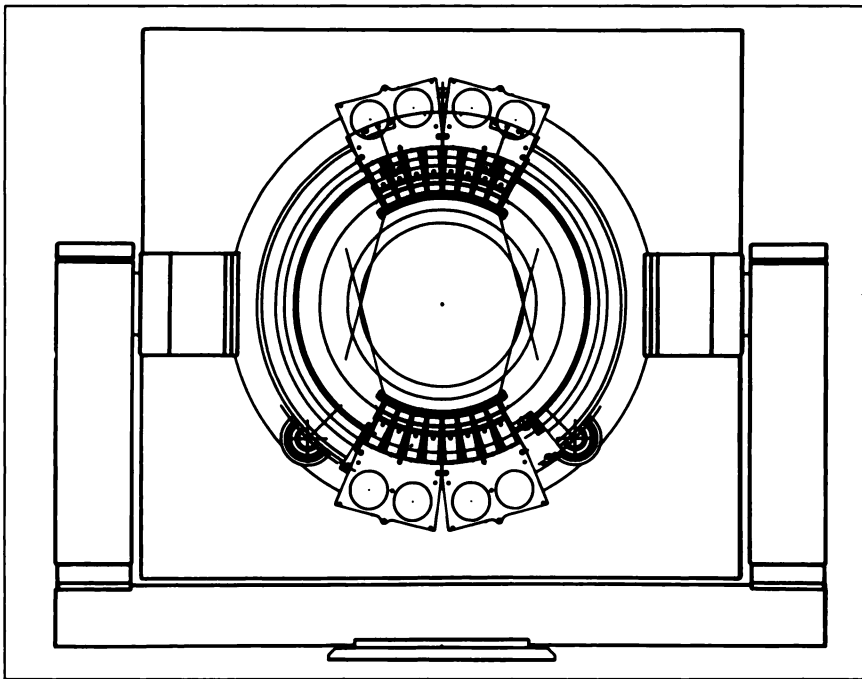
FIGURE 1. Schematic of the scanner showing the two sets of buckets mounted on the rotating support.

edge of the projection. The transaxial sensitivity profile is therefore a maximum at the center of the FOV, although this effect is to some extent offset by attenuation, which is also usually a maximum near the center of the FOV.

In the current prototype, data are acquired at 6, 12, 24 or 48 consecutive angular positions with rotational steps of 30° (one bucket), 15°, 7.5° and 3.75°, respectively. The corresponding fields of view are 20.2, 30.1, 35 and 37.5 cm.
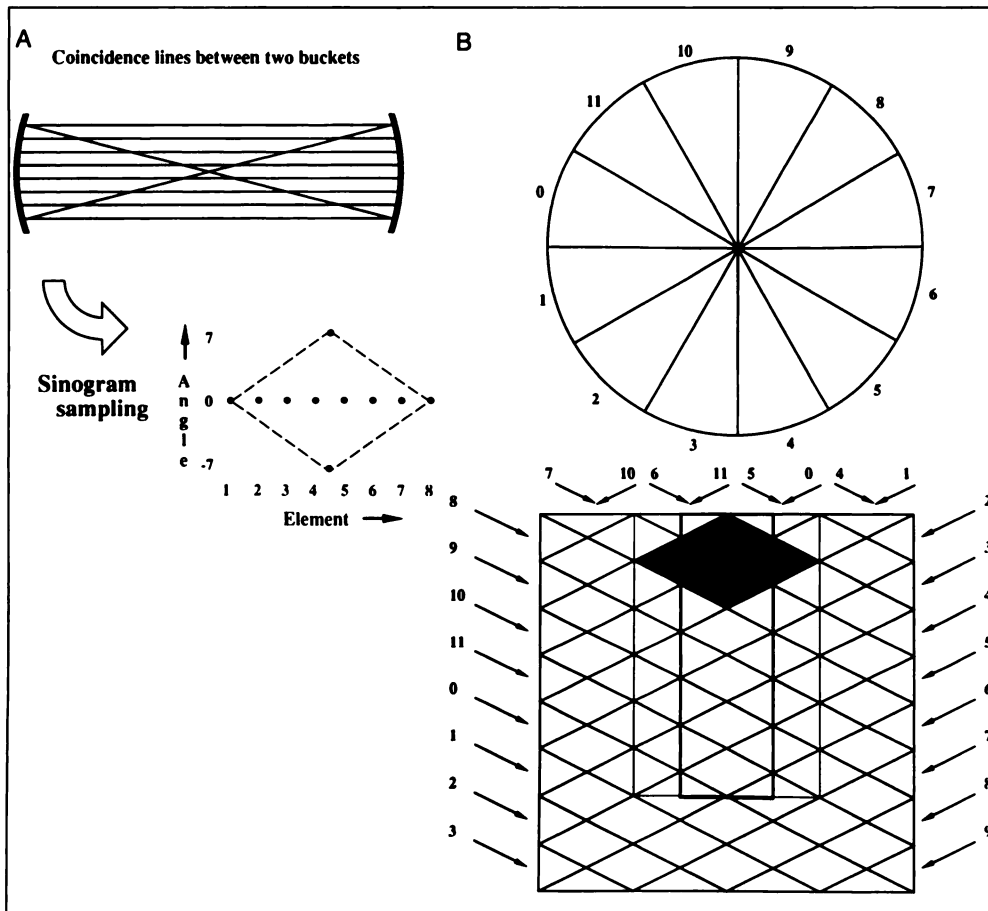

FIGURE 2. (A) A simplified diagram showing LORs between two groups of 8 detectors in a bucket. The measured LORs form a diamond-shaped region on the sinogram with axes of 8 elements by 15 angles. The LORS corresponding to angles of 0 and ±7 are indicated on the sinogram diamond. (B) The four sinogram diamonds acquired at a single position of the scanner. The numbers correspond to the 12 possible bucket positions around the ring as shown. The region indicated is for buckets at positions (0,1) in coincidence with buckets at positions (6,7). The diamonds along the diagonal numbered, for example, 2, contain all the LORs between the bucket in position 2 and any other bucket position.

Data Acquisition

Data acquisition is controlled from a SUN SparcStation 2 computer. Standard VME-based, CTI acquisition electronics for coincidence processing and sorting are used. Data are acquired at each angle for a preset time. For this prototype, no acquisition is performed during the rotation of the detectors. When acquisition is completed for the first angle, the detectors move to the second position. Acquisition then starts into a second buffer during which data from the first buffer are corrected for detector efficiency differences, deadtime, isotope decay and any small variations in acquisition time, and then assembled into the sinogram buffer. Appropriate weighting factors correct for more than one detector pair contributing to the same LOR. Detector efficiency correction factors are obtained in the usual way from a scan of a plane source with high statistics, with the detectors in a fixed position. Real-time correction of each LOR is necessary because coincidences from different detector pairs that contribute to the same LOR are summed during acquisition. When the acquisition is complete, the corrected sinograms are written to disk. A complete set of 256 sinograms requires 6.5 Mbytes of storage.

The rotational motion of the detectors is controlled by a commercial stepper-motor controller (Centroid MC8). The minimum rotational step is 0.002° and the angular step corresponding to one detector is 0.93°.

The minimum total scan duration is determined by the time to both process the data from the acquisition buffer to the sinogram buffer and to move the detectors from one acquisition position to the next. This is currently 5 sec per angle for processing and an average of about 6°/sec for detector motion. For a 20-cm FOV, six acquisition positions are required, resulting in a minimum possible scan duration of 55 sec, comprising 30 sec of data acquisition and 25 sec of rotation, i.e., a scanning efficiency of 55%. This efficiency improves as the scan time increases and the fraction of total time spent moving the detectors decreases, e.g., for a 10-min acquisition the efficiency is 96%.

In view of the potential of the scanner to perform 60-sec scans, dynamic imaging of FDG uptake in the brain and heart has also been investigated. The current protocol adopted for a brain study consists of 5 scans of 60 sec, 4 scans of 120 sec, 2 scans of 240 sec, 1 scan of 300 sec and 3 scans of 600 sec. The final three scans can be summed to provide the equivalent of a single static scan of 30 min.

Attenuation Correction

For this scanner, transmission scans are obtained by attaching a 6-mm thick solid germanium plane source to the front of one array of detectors. The source, which is 10.8 cm wide to cover the entire axial field of view, rotates with the detectors. When filled initially, the source contained 33 MBq of ^{68}Ge and the proximity of the source to the detectors results in large deadtime correction factors for that detector array (e.g., 35% deadtime).

Brain studies are corrected for attenuation using an ellipse approximation for the head and a constant attenuation coefficient ($\mu = 0.095$ per cm). The plane source is used for whole-body studies in cardiology and oncology. To reduce the effect of noise in the transmission scan, a set of two-dimensional transmission images are first reconstructed from the blank and transmission scans. These images are segmented into regions (e.g., air, soft tissue and lung) with preassigned uniform attenuation coefficients, after which the complete three-dimensional set of attenuation correction factors is generated by forward projection through the segmented images.

Scatter Correction

The septa in a multi-ring scanner shield the detectors from out-of-plane scatter. This is particularly important when the scanner is operated with a lower energy threshold well below the photopeak, e.g., at 250 keV. Scatter contributes a nonlinear, slowly varying background to the reconstructed image. For this scanner, the measured sinograms are corrected for scatter before reconstruction using an iterative convolution-subtraction method originally developed for SPECT (21) and recently applied to PET data. First, a subset of two-dimensional projections $p_{md}(s, \hat{u})$ are formed from the measured (m) direct (d) plane sinograms only, where $\hat{u}$ is the projection direction and s is the two-dimensional coordinate within the projection plane. Each of these two-dimensional projections is then convolved with the scatter kernel:

$$k(s, \hat{u}; \alpha, \beta) = \frac{\alpha}{(1 - \alpha)} e^{-\beta s}, \qquad \text{Eq. 1}$$

where $s = |s|$.

The parameters α (scatter fraction) and β (slope of the scatter tail) are obtained from line source measurements in an appropriate scattering medium. A first estimate of the scatter corrected projections is then obtained from:

$$p_c^0(s, \hat{u}) = p_{md}(s, \hat{u}) - p_{md}(s, \hat{u})^*k(s, \hat{u}; \alpha, \beta) \qquad \text{Eq. 2}$$

where * denotes two-dimensional convolution in the s variable. A better estimate of scatter is now obtained by convolving the corrected projection $p_c^0(s, \hat{u})$ with $k(s, \hat{u}; \alpha, \beta)$ and then subtracting this estimate from the measured projections $p_{md}(s, \hat{u})$. This procedure can be repeated; at each iteration, the scatter is estimated by convolving the scatter kernel with the corrected projections from the previous iteration. Typically, three to four iterations are found to be sufficient. The scatter estimate obtained in this way from the direct projections is also subtracted from oblique projections on the assumption that scatter will not vary significantly with small changes in the projection angle.

Image Reconstruction Procedure

This reconstruction algorithm is identical to that developed for the ECAT 953B with septa retracted. The details and results of this work have been fully discussed (14). The algorithm is based on the approach described by Kinahan and Rogers (15).

Since the rotating camera has no septa, coincidence data from up to 8 million LORs are acquired during a scan. As previously described (14), these LORs form a set of about 4500 measured two-dimensional parallel projections, $p_m(s, \hat{u})$, where s and $\hat{u}$ are defined above. However, the truncated cylindrical geometry of the camera results in the two-dimensional projections at oblique angles only partially measured. As suggested by Pelc (22), the unmeasured parts of the oblique projections can be obtained by forward projection through an initial estimate of tracer distribution. This estimate is based on two-dimensional reconstructions of the conventional set of slices that are then stacked to give a three-dimensional volume. The unmeasured LORs are obtained by forward projection through this volume (15).

Thus, with the exception of the direct projections, each of the complete two-dimensional projections $p(s, \hat{u})$ is composed of both measured ($p_m(s, \hat{u})$) and forward projected elements. These projections are filtered with a two-dimensional filter function $h(s, \hat{u})$ [see for example, Colsher (6)]:

$$p_F(s, \hat{u}) = \iint d^2s' p(s', \hat{u}) h(s - s', \hat{u}) \qquad s'.\hat{u} = 0$$

$$= p(s, \hat{u}) * h(s, \hat{u}), \qquad \text{Eq. 3}$$

where $p_F(s, \hat{u})$ is the filtered projection. Since the scanner has cylindrical symmetry, the filter $h(s, \hat{u})$ will be independent of the azimuthal angle. The filtered projections are then backprojected into the three-dimensional volume to give the reconstruction (16):

$$f(x) = \iint_\Omega d^2\hat{u} \, p_F(x - (x.\hat{u})\hat{u}, \hat{u}), \qquad \text{Eq. 4}$$

where Ω is the geometrical acceptance of the scanner, i.e., $\hat{u} \in \Omega$.

RESULTS

Scanner Performance

Spatial Resolution. Spatial resolution has been measured with a line source in air. Transaxial resolution is 5.7 mm (tangential) and 5.9 mm (radial) at the center, and 6.5 mm (tangential) and 6.8 mm (radial) at 10 cm from the center. Mean axial resolution (FWHM) is 5.4 mm (center of FOV) and 6.4 mm (at 9 cm); the FWTM are 12.5 and 14.1 mm, respectively.

Sensitivity. Absolute sensitivity is defined as the number of photon pairs detected by the scanner expressed as a percentage of the total number of positrons emitted from the source. By using the procedure of Bailey et al. (23) to correct for source attenuation, the absolute sensitivity of the prototype was measured to be 0.51% for a line source at the center of the FOV, with an energy threshold of 250 keV. The same measurement for the 953B with septa extended is 0.63%. The randoms-subtracted count rate measured with a 20-cm diameter uniform cylinder (15 cm long) containing an activity concentration of 37 kBq/ml (i.e., 1 μCi/ml) is 148,000 cps as compared with 152,000 cps for the 953B with septa extended. The scatter subtracted count rates are 90,000 cps and 133,000 cps for the rotating scanner and the 953B with septa extended, respectively.

Scatter Correction. The energy resolution for this block is 23% (s.d.) and the camera is operated at a lower energy threshold of 250 keV. The scatter fraction (integrating within the scattering medium) estimated from a centered line source in a 20-cm water phantom is 35%. The corresponding estimate for the 953B with septa extended is 12% (20). Brain studies are corrected using the convolution-subtraction procedure with a monoexponential scatter kernel (scatter fraction $\alpha = 0.32$, slope $\beta = 0.051$ per cm).

We have validated this approach for scatter correction using a phantom consisting of a 20-cm diameter uniform cylinder within which two smaller diameter cylinders are positioned. The inner cylinders contain activities of zero (cold) and 3.8 (hot) relative to the (warm) activity in the large cylinder. The phantom is imaged and reconstructed both with and without scatter correction. The reconstructed activity in the cold cylinder relative to the warm background decreased from 31% to 4% after scatter correction, and the ratio of activity in the hot cylinder relative
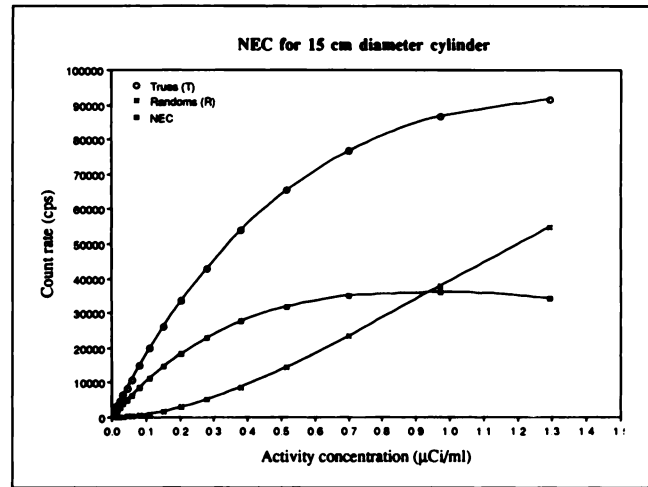

FIGURE 3. The trues and randoms rates and the noise equivalent count rate as a function of activity concentration for a 15-cm diameter, uniform cylinder.

to background increased from 2.9 to 3.4 after scatter correction, which is closer to the well-counter value of 3.8.

Noise Equivalent Count Rate. The noise equivalent count rate (NEC) can be calculated from (24):

$$NEC = \frac{T^2}{(T + S + 2fR)}, \qquad \text{Eq. 5}$$

where T, S and R are the trues, scatter and randoms rates, respectively, and f is the fraction of the projection subtended by the object. The factor of 2 in the denominator accounts for the increase in noise arising from the randoms correction procedure (subtraction of a time-delayed coincidence map). This expression assumes that either the scatter correction procedure is noiseless or that no correction for scatter is applied. The NEC provides useful insight into the performance characteristics of a particular scanner. However, since it does not take into account other parameters such as spatial resolution, it is less useful for comparing different types of scanners. Bailey et al. (25) have measured NECs for the 953B in a variety of different imaging situations, including human studies.

For this scanner with an energy threshold at 250 keV, the NEC has been measured for both a 15-cm and a 20-cm diameter uniform cylinder as a function of activity concentration. As shown in Figure 3 for the 15-cm diameter cylinder, the NEC reaches a maximum of 36,000 cps with a concentration of 26 kBq/ml at a trues rate of 80,000 cps, 28% randoms and a scatter fraction of 23%. For the 20-cm cylinder, the NEC reaches a maximum of 17,000 cps with an activity concentration of 20 kBq/ml at a trues rate of 62,000 cps, 35% randoms and a scatter fraction of 35%.

Image Reconstruction. Fully three-dimensional image reconstruction is performed on an i860-based, 80 Mflop SuperCard II (CSP Inc., Billerica, MA), which is located in the VME crate with the acquisition electronics. For calculated attenuation correction, the full set of correction factors are obtained by forward projection, a procedure which
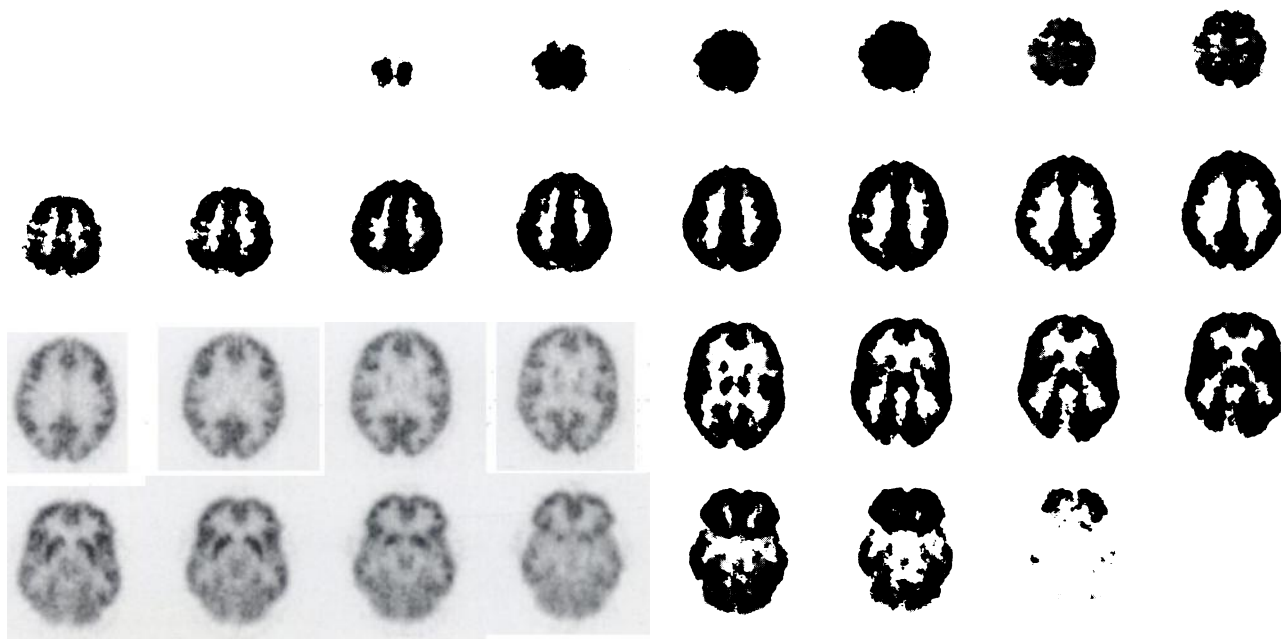
FIGURE 4. A 20-min brain scan in a normal volunteer 45 min after injection of 260 MBq of [18]FDG. The images show 31 transverse sections, 3.3 mm thick, starting at the apex of the brain.

takes about 1 min. Forward projection of 170 unmeasured sinograms takes 8 min, and filtering and backprojection of the two-dimensional projections takes an additional 11 min. The full reconstruction (with overheads) takes 22 min. This time could be reduced by about 30% by using a new reconstruction algorithm (26) which eliminates the forward projection step.

Imaging Applications. The scanner has been validated by imaging some standard phantoms and by performing a variety of clinical studies in humans using [18]FDG and [82]Rb.

Figure 4 shows a brain study obtained from a normal volunteer. The transverse images are 3.3 mm thick and were acquired 45 min after a 260-MBq injection of FDG for a scan time of 20 min. The images exhibit excellent spatial resolution with clear separation of the cerebral hemispheres in the superior sections and good definition of the sub-cortical structures. A typical FDG brain study following a 260-MBq injection of FDG results after 45 min in a prompt coincidence rate of about 50,000 cps with 10% randoms and 22% deadtime. Two neurological patient studies are presented in Figure 5. Figure 5A shows a 50-yr-old female patient with an infarct affecting the anterior pole of the left thalamus; the lesion is clearly visible on the PET scan and corresponds to a 30% decrease in glucose metabolism compared with the contralateral region of the right thalamus. Figure 5B shows a patient with right temporal lobe epilepsy; the patient has subsequently undergone surgical resection of the inferior pole of the right temporal lobe and has been seizure-free for over 6 mo. For both studies, the scan time was 40 min, each scan commencing 45 min after injection of 220 MBq of FDG.
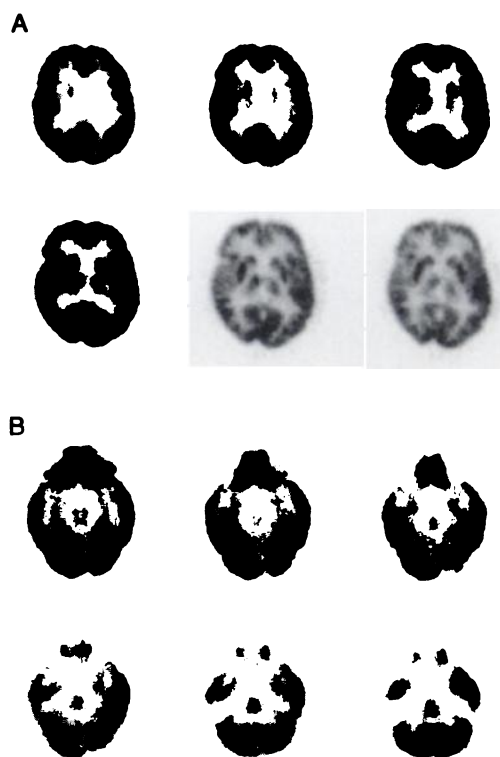

FIGURE 5. Fluorine-18-FDG brain studies in patients. (A) Six transverse sections through the brain at the level of the thalamus in a patient with a hypometabolic lesion in the left anterior thalamic region and (B) six transverse sections at the level of the temporal lobes in a patient with temporal lobe epilepsy; the scan was performed interictally. The sections are 3.3 mm thick and the scan time was 40 min for each study.
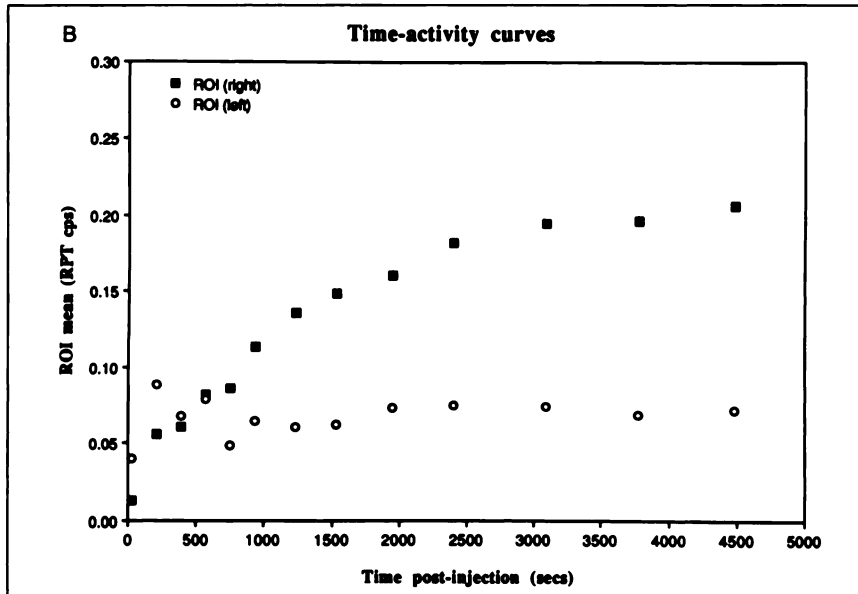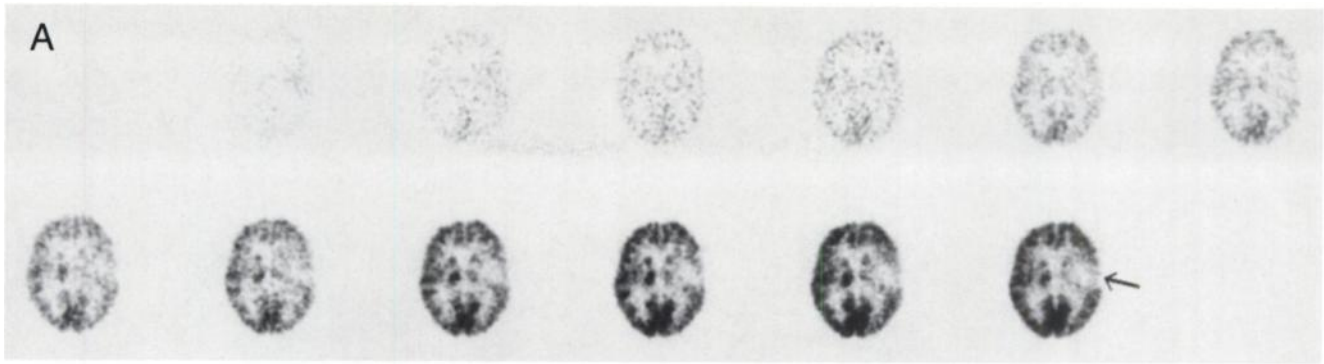
FIGURE 6. A 13-frame dynamic [18]FDG brain scan in a patient with a large arteriovenous malformation affecting the left parietal cortex (arrowed). (A) Plane 11 for each of the 13 time frames and (B) the time-activity curves for two ROIs, one in the region affected by the malformation (lower curve, circles) and the other in the same region on the contralateral cortex (upper curve, squares). Note the early peak in the lower curve due to the transit of blood through the malformation and the subsequent significantly-reduced cortical metabolism. The metabolism on the contralateral side appears normal.

A 13-frame dynamic brain scan is shown in Figure 6. The patient has a large arteriovenous malformation affecting the left parietal cortex (arrowed). A single section (plane 11) is displayed in Figure 6A for each of the 13 time frames, and in Figure 6B the time-activity curves are plotted for two regions of interest (ROIs), one in the region affected by the malformation (lower curve) and the other in the same region on the contralateral cortex (upper curve). The metabolic deficit due to the malformation is clearly demonstrated.

Imaging of the myocardium is illustrated in Figure 7 for a normal volunteer and a patient with an infarct in the anterior wall. The transaxial sections are 3.3 mm thick and the acquisition time was 30 min for each view. For myocardial imaging, a 300-MBq injection of FDG results in a prompt coincidence rate of 43,000 cps with 35% randoms and 30% deadtime. Cardiac imaging with [82]Rb is illustrated in Figure 8 for a patient with an inferior wall infarct. The patient was infused with 925 MBq of [82]Rb from a commercial rubidium infusion system. Sixty seconds after the end of infusion, a single rotation, 300-sec scan was performed during which approximately five million counts were acquired. The maximum count rate at the start of imaging

was 90,000 cps with 50% randoms. The section thickness is 6.6 mm. The images show a region of low flow (arrowed) in the inferioposterior wall of the myocardium.

Finally, oncology applications are illustrated by the two studies shown in Figure 9. Three frontal sections are shown in Figure 9A through the neck of a patient with a tumor of the sinus piriforme. The sections are 1.5 mm thick and are viewed facing the patient. The primary tumor appears as a centrally located focal uptake (arrowed), while the uptake to the patient's right is due to secondary involvement of lymph nodes. The base of the cerebellum is seen at the top of each section. These images were obtained by performing two contiguous scans covering a total axial length of 20 cm. Note the low level of nonspecific uptake of FDG in this region. In the second study, Figure 9B, the images are three 3.3-mm thick transaxial sections through the abdomen at the level of the liver in a patient with liver metastases. For this patient, a 180-MBq injection of FDG resulted in a prompt coincidence rate of 22,000 cps with 20% randoms and 20% deadtime. The regions showing increased uptake of FDG are about 6 mm in size and were reported as inconclusive from CT. Subsequent biopsy confirmed the presence of malignancy. Note the low
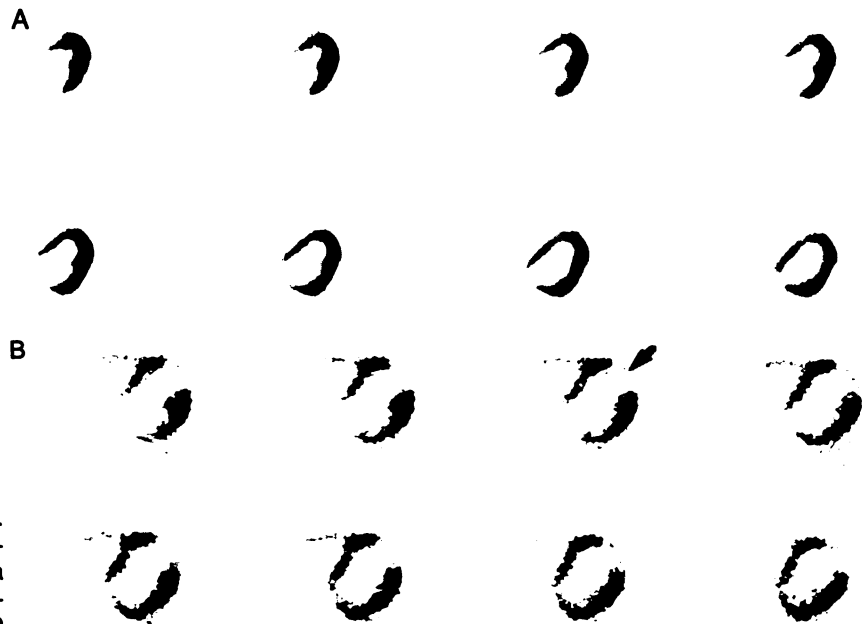
FIGURE 7. Myocardial imaging with FDG. (A) Eight transverse sections in a normal volunteer and (B) eight transverse sections in a patient with an infarct in the anterior wall (arrowed). For each study, the scan time was 30 min and the scan was performed 45 min after an injection of 260 MBq of [18]FDG.

uptake of FDG in the surrounding normal liver tissue, which results in target-to-background ratios greater than 3 for malignant tumors.

DISCUSSION

With the exceptions of reduced sensitivity and the need to rotate the detectors during acquisition, it is clear from the performance parameters and representative images presented here that scanner performance is comparable to the full-ring equivalent. Axial and transaxial spatial resolution are similar to the 953B and are clearly not degraded by the mechanical movement of the detectors.

The absolute sensitivity at the center of the FOV as measured by the method of Bailey et al. (23) is 0.5%, which is 23% lower than the 953B with septa extended. For a 20-cm phantom, the sensitivity is 3% lower than the 953B (septa extended) without scatter subtraction and 47% lower after subtracting scatter. The difference in sensitivity between the rotating scanner and the 953B is greater for the cylinder (47%) than for the line source (23%) because the sensitivity of the rotating scanner decreases away from the center in both the axial and transaxial direction, whereas for the 953B with septa extended it is essentially constant throughout the FOV. Because the rotating scanner does not have septa, operation with low levels of activity in the FOV is preferred. The maximum NEC for a 15-cm diameter uniform cylinder is 36,000 cps at an activity concentration of 26 kBq/ml. The maximum NEC for the same phantom in the 953B, with and without septa is 150,000
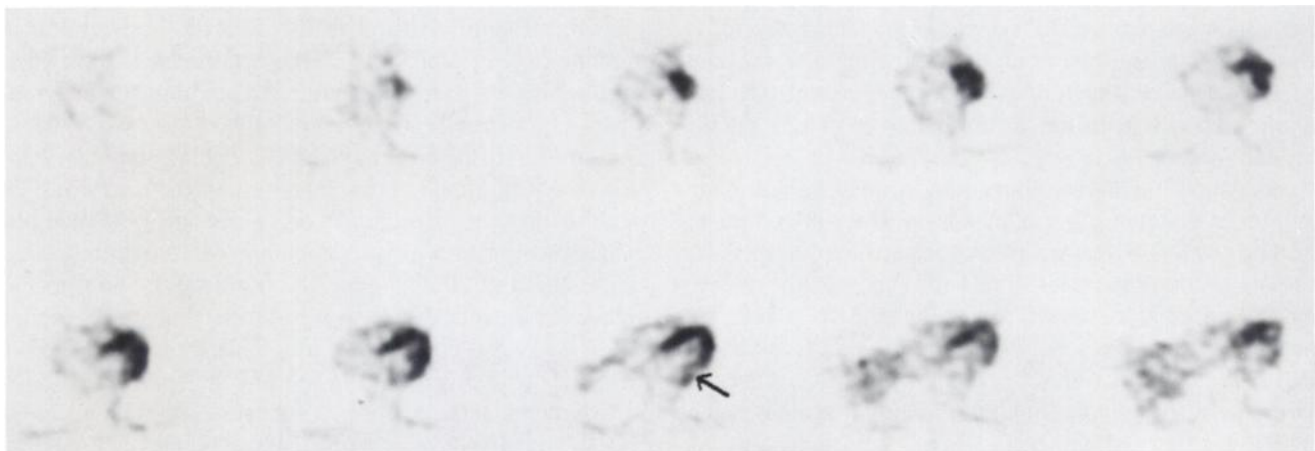

FIGURE 8. Myocardial imaging with [82]Rb. A patient with an inferior myocardial infarct was infused with 925 MBq of [82]Rb from a commercial rubidium infusion system. Sixty seconds after the end of infusion, a single, 300-sec scan was performed during which approximately five million counts were acquired. The maximum total count rate at the start of imaging was 90,000 cps, with 50% randoms. The section thickness is 6.6 mm. The images reveal a region of low flow (arrowed) in the inferio-posterior wall.
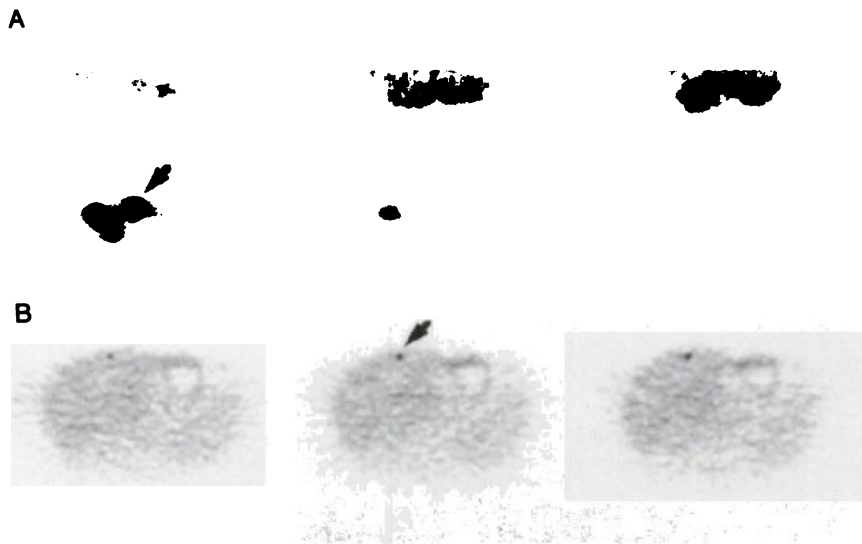
A

B

FIGURE 9. Fluorine-18-FDG in oncology. (A) Three frontal sections through the neck of a patient with a tumour of the sinus piriforme. The sections are 1.5 mm thick and are viewed facing the patient. The primary tumor appears as a centrally located focal uptake (arrowed), whereas the uptake to the patient's right is due to secondary involvement of lymph nodes. The base of the cerebellum is seen at the top of each section. The images were obtained by performing two contiguous scans covering a total axial length of 20 cm and (B) transverse sections 3.3 mm thick through the abdomen at the level of the liver in a patient with liver metastases. The scan demonstrates strong focal uptake. The metastasis (arrowed) was a 6-mm lesion reported as inconclusive on CT. Note the low uptake in normal liver tissue.

cps, which is achieved at concentrations of 29 kBq/ml (septa retracted) and 220 kBq/ml (septa extended) (*25*).

The average scatter fraction for a line source in a 20-cm scattering medium is 35%, which, as expected, is a threefold increase over the 953B with septa extended and is about the same as the 953B with septa retracted. Despite the large scatter fraction and the obvious approximations implicit in the correction procedure, it is encouraging that the convolution-subtraction approach seems to be effective in correcting for scatter in the reconstructed images, improving contrast and quantitation, i.e., the ratio between regions of different tracer concentration.

As mentioned above, more than one detector pair may contribute to an LOR during a scan. Although this effect can be corrected by simple weighting factors, it will nevertheless result in a nonuniform noise distribution across the sinogram. However, as a result of the averaging effect of the backprojection process, for typical count densities encountered in PET images, no related noise structure has been observed in the reconstructed image. This has been verified for a uniform cylinder by both simulation and measurement and may also be related to the opposing effects of increased counts due to increased sensitivity and decreased counts due to photon attenuation.

An important feature of this scanner is the intrinsic three-dimensional nature of the data acquisition and reconstruction. The use of septa and two-dimensional data acquisition would have resulted in too low a sensitivity for the scanner to be used for clinical applications. The image quality obtained for the patient studies shown in Figures 4–9 validate this approach. The recent development of efficient three-dimensional reconstruction algorithms has obviously been essential.

It is well-known that a major advantage of PET is its potential to quantitate both flow and metabolism in vivo. The use of a rotating camera with very short-lived radioisotopes, such as ^{15}O, may be difficult because a steady-state tracer distribution (isotope decay excepted) must be ensured throughout the rotation of the scanner. Even so, the results with rubidium (75-sec half-life) for imaging flow in the myocardium have been encouraging. The rubidium images were acquired with a single rotation of the camera which took 300 sec, i.e., 25 sec of acquisition per angle. As for the FDG studies, the data were corrected on-line for deadtime and decay. The correction factor for the rubidium studies varied from typically 3 at the start (deadtime) up to 25 at the end (isotope decay). Despite the large variation in true counts at each angle during the scan, no obvious artifacts were identified in the images. Protocols that smooth out variations in count rate would require multiple contiguous rotations which are not feasible with the current prototype.

By imaging FDG uptake 45 min after injection and applying the standard static FDG model (*27*), this scanner has been used successfully to measure regional cerebral glucose metabolism in both patients and normal volunteers. Estimation of glucose metabolic rates by fitting dynamic time-activity curves, such as that shown in Figure 6B, is currently being explored. To date, we have found considerable clinical interest for the investigation of ENT, lung and abdominal tumors, especially for staging, monitoring the efficacy of treatment and identifying postoperative tumor recurrence.

All the studies performed with this scanner used tracers obtained on a weekly basis from a remote cyclotron. Clearly, the combination of a relatively inexpensive, rotating PET scanner and a centralized isotope production facility represents a powerful addition to clinical imaging modalities such as MRI and SPECT that are more widely available. In an established PET center, a rotating scanner could complement a full-ring scanner by performing many of the more clinical studies, thus allowing the full-ring scanner to concentrate on research-oriented applications.

CONCLUSIONS

We have presented the design and performance characteristics of a new, lower-cost PET scanner based on the rotation of BGO block detectors. To date, the scanner has performed over 180 studies in patients using ^{18}FDG transported from a remote cyclotron and ^{82}Rb from a commercial generator. We feel that the quality of these studies, both static and dynamic, compare favorably with an equivalent full-ring scanner operated with septa. A large fraction of the studies have been applications in oncology, for which this type of camera is well suited. The limited 10-cm axial field of view is being addressed in a second prototype which is currently under construction. The new scanner will have an axial FOV of 15 cm (3 blocks wide) and will also offer increased sensitivity for imaging the brain and heart.

Although the rotation of detector arrays for positron tomography is not a new idea, this is the first time it has been applied to state-of-the-art, BGO block detectors using fully three-dimensional data acquisition. The success of the current prototype for patient studies represents an important step in taking PET into the clinical environment.

ACKNOWLEDGMENTS

REFERENCES

1. Muehllehner G, Atkins F, Harper PV. Positron camera with longitudinal and transverse tomographic capabilities. In: Medical radionuclide imaging, volume 1. Vienna: IAEA; 1977:291–307.
2. Brownell GL, Burnham CA, Chesler DA, et al. Transverse section imaging of radionuclide distributions in heart, lung and brain. In: Reconstruction tomography in diagnostic radiology and nuclear medicine. [Ter-Pogossian, MM, Phelps ME, Brownell GL, Eds] Baltimore: University Park Press; 1977:293–307.
3. Paans AMJ, Vaalburg W, Woldring MG. A rotating double-headed positron camera. J Nucl Med 1985;26:1466–1471.
4. Marsden PK, Ott RJ, Bateman JE, et al. The performance of a multiwire proportional chamber positron camera for clinical use. Phys Med Biol 1989; 34:1043–62.
5. Townsend DW, Frey P, Jeavons A, et al. High density avalanche chamber (HIDAC) positron camera. J Nucl Med 1987;28:1554–1562.
6. Colsher JG. Fully three-dimensional positron emission tomography. Phys Med Biol 1980;25:103–115.
7. Schorr B, Townsend DW, Clack R. A general method for three-dimensional filter computation. Phys Med Biol 1983;28:305–312.
8. Defrise M, Kuijk S, Deconinck F. A new three-dimensional reconstruction method for positron cameras using plane detectors. Phys Med Biol 1988; 33:43–51.
9. Ott RJ, Marsden PK, Flower M, et al. Clinical PET with a large area multiwire proportional chamber PET camera. Nucl Instrum Meth 1988; A269:436–442.
10. Frey PE, Townsend DW, Flattet A, et al. Tomographic imaging of the human thyroid using ^{124}I. J Clin Endocrinol Metab 1986;63:918–927.
11. McKee BTA, Hogan MJ, MacPhail JD. Data acquisition for a medical imaging MWPC detector. Nucl Instrum Meth 1991;A310:545–551.
12. Tavernier S, Bruyndonckx P, Shuping Z. A fully 3D small PET scanner. Phys Med Biol 1992;37:635–643.
13. Suckling J, Ott RJ, Marsden PK, et al. A prototype BaF$_2$/TMAE low pressure multiwire proportional chamber for PET. IEEE Trans Nucl Sci 1991;NS-38;703–708.
14. Townsend DW, Geissbuhler A, Defrise M, et al. Fully three-dimensional reconstruction for a PET camera with retractable septa. IEEE Trans Med Imaging 1991;MI-10:505–512.
15. Kinahan PE, Rogers JG. Analytic three-dimensional image reconstruction using all detected events. IEEE Trans Nucl Sci 1990;NS-36:964–968.
16. Defrise M, Townsend DW, Geissbuhler A. Implementation of three-dimensional image reconstruction for multi-ring positron tomographs. Phys Med Biol 1990;35,10:1361–1372.
17. Townsend DW, Wensveen M, Byars L, et al. A rotating PET camera using BGO block detectors. Conference Records of the 1991 IEEE Nuclear Science Symposium 1992;2:1658–1662.
18. Townsend DW, Defrise M. Reconstruction methods in positron tomography. Report CERN 93-02. Geneva, Switzerland:1993.
19. Casey ME and Nutt R. A Multicrystal two-dimensional BGO detector system for positron emission tomography. IEEE Trans Nucl Sci 1986;NS-33:460–463.
20. Spinks TJ, Jones T, Bailey DL, et al. Physical performance of a positron tomograph for brain imaging with retractable septa. Phys Med Biol 1992; 37:1637–1655.
21. Bailey DL, Hutton BF, Meikle SR, Fulton RR, Jackson CB. Iterative scatter correction incorporating attenuation data. Eur J Nucl Med 1989;15: 452.
22. Pelc NJ. A computerized filtered backprojection algorithm for three dimensional reconstruction. PhD thesis, Harvard School of Public Health, Boston, MA. 1979:140.
23. Bailey DL, Spinks TJ, Jones T. A method for measuring the absolute sensitivity of positron emission scanners. Eur J Nucl Med 1991;18:374–379.
24. Strother SC, Casey ME, Hoffman EJ. Measuring PET scanner sensitivity— relating count rates to image signal-to-noise ratios using noise equivalent counts. IEEE Trans Nucl Sci 1990;37:783–788.
25. Bailey DL, Jones T, Spinks TJ, Gilardi MC, Townsend DW. Noise equivalent count measurements in a neuro-PET scanner with retractable septa. IEEE Trans Med Imaging 1991;MI-10,3:256–260.
26. Defrise M, Townsend DW, Clack R. FaVoR: a fast reconstruction algorithm for volume imaging in PET. IEEE Medical Imaging Conference Record 1992;3:1919–1923.
27. Phelps ME, Huang SC, Hoffman EJ, et al. Tomographic measurement of local cerebral glucose metabolic rate in humans with (F-18)2-fluoro-2-deoxy-D-glucose: validation of method. Ann Neurol 1979;6:371–388.